Nanosensor Chemical Cytometry for Characterizing the Efflux Heterogeneity of Nitric Oxide from

Macrophages

Soo-Yeon Cho, Volodymyr B. Koman, Xun Gong, Sun Jin Moon, Pavlo Gordiichuk, Michael S. Strano*

Department of Chemical Engineering, Massachusetts Institute of Technology, Cambridge, MA 02139, United States

*Corresponding author: strano@mit.edu

KEYWORDS: macrophage, nitric oxide, heterogeneity, microfluidics, cellular lensing, nanosensor

ABSTRACT

Macrophages are a critical part of the human immune response, and their collective heterogeneity is implicated in disease progression and prevention. There currently does not exist a non-destructive, label-free tool for profiling the dynamic, antigenic responses of single macrophages in a collection to correlate with specific molecular expression and correlated biophysical properties at the cellular level, despite the potential for diagnosis and therapeutics. Herein, we develop a nanosensor chemical cytometry (NCC) that can monitor the heterogeneity of inducible nitric oxide synthase (iNOS) responses from macrophage populations. By integrating near infrared (nIR) fluorescent nanosensor array with microfluidics, unique cellular lensing effect of macrophage was utilized to characterize both nitric oxide (NO) efflux and refractive index (RI) changes in single cell level. Using a parallel, multi-channel approach, distinct iNOS heterogeneities of macrophages can be monitored at attomolar (10⁻¹⁸ moles) sensitivity in a nondestructive and real-time manner with a throughput of exceeding the 200 cells/frame. We demonstrate that estimated mean NO efflux rates of macrophage populations are elevated from $342 (\sigma = 199)$ to $464 (\sigma = 206)$ attomole/cell·hr with a 3% larger increase in the heterogeneity, and estimated RI of macrophage decrease from 1.366 ($\sigma = 0.015$) to 1.359 ($\sigma = 0.009$) with trimodal subpopulations under lipopolysaccharide (LPS) activation. These measured values are also in good agreement with Griess assay results and previously reported measurements. This work provides a unique strategy for single cell analysis of macrophage populations for cellular immunology and biopharmaceutical research.

Reactive nitrogen species (RNS) including nitric oxide (NO) play significant roles in numerous physiological processes as biochemical signaling molecules and as a part of the respiratory burst in the immune responses.^{1,2} Immune cells such as macrophages exhibit considerable cell-to-cell heterogeneity in terms of expression levels of inducible nitric oxide synthase (iNOS) in inflammation response to infection.^{3,4} This has complicated the connection between the overall immune response and the genomic and proteomic characteristics of individual macrophages.⁵ There is a pressing need for technology that can bridge the detection of single cell phenotypes of statistically significant cell populations to understand and characterize collective responses. 6 The ability to analyze individual living cells means that multiplex diagnostics are enabled in series, a workflow that is necessary to address the problems of cellular complexity. In this work, we adapt a recent advance from our laboratory that we call Nanosensor Chemical Cytometry (NCC), based on an array of fluorescent nanosensor integrated along a microfluidic channel. The lensing effect of the flowing cells allows for rapid extracting single cell information, and correlating biomolecular information with physical properties. We show that the upgraded NCC platform can be utilized to label-free monitor the NO expression level of single macrophage correlating with unique optical properties.

Macrophages are widely distributed in the body with differences in their origin and are brought together by external factors and the internal local environment.⁸ Accordingly, they respond to environmental changes in a highly heterogeneous manner to affect physiological and pathological processes.⁵ Immune-stimulated macrophages phagocytose pathogens and cell debris, orchestrate tissue repair, and resolution of tissue injury by delicate RNS control based on iNOS.⁹ On the other hands, this RNS efflux also can damage the normal tissue cells to generate pathogenic effects, and is widely involved in the development of various metabolic, cardio vascular and

neurodegenerative diseases.¹⁰⁻¹² Thus, subtle molecular differences at the RNS level of macrophage populations can represent significantly different immune states.¹³ Therefore, a tool that would enable the profiling of dynamic antigenic response of single macrophage and eventually molecular heterogeneities as function of different biophysical properties could aid in our systematic understanding of the immune mechanism to unknown microorganisms and the progression of these diseases, eventually leading to promising future therapeutics.^{14,15} However, the accurate determination of single cell RNS efflux is a significant challenge because of its low concentration (10⁻¹⁸ to 10⁻¹⁵ mole level)) and transient half-life on the order of milliseconds to seconds with rapid diffusion and reaction due to interference by other chemicals (glucose, nitrites, thiols) in biological media.^{16,17}

Chemical cytometry has been widely used to quantify this RNS molecular heterogeneities of immune cell populations allowing quantitative information to be gathered with high selectivity. ^{18,19}. Cells are pre-labelled, lysed, and separated to detect the intra- and extra-cellular NO components during the process. ²⁰⁻²² Even though chemical cytometry is a well-established and can provide single-time-point measurements of multiple parameters, it is critically limited by the fact that cells must be kept in suspension with pre-labeling, destroyed, and that there is no way to track individual cells across multiple time points, which is inadequate for monitoring of immune response mechanism of macrophage populations. ²³

Nanotechnology-based monitoring tools including fluorescent nanosensors,^{24,25} field-effect transistor,²⁶ and electrochemical devices^{27,28} have shown significant potential to label-free RNS profiling of cell populations in non-destructive way. Their rapid and real-time sensitive opto-electronic signal readout and tunable chemical selectivity are ideal for this purpose.²⁹⁻³² However, extending these nanosensor devices to the monitoring of statistically relevant numbers of immune

cells remains unaddressed to date with the basic problem of low-spatial resolution, cell imaging and designation method, sensor interfacing strategy, and signal transducing mechanism.^{7,33}

In this work, we developed a fluorescent nanosensor array integrated microfluidics that can characterize the NO efflux heterogeneities of macrophage populations. Near infrared (nIR) fluorescent single-walled carbon nanotube (SWNT) array was uniformly integrated within a macrophage incubating microfluidic channel. Each single macrophage optically interacts with the underlying NO nanosensor array, producing an informative nIR optical lensing profile that can be modeled as a photonic nanojet. Within this biophotonic waveguide, macrophages can be both visualized and chemically tracked in real-time and at high-resolution, without the need for labeling or additional optical manipulation. Based on the combination of nanosensor response and observed cellular lensing properties, our platform is able to inform the heterogeneities of macrophage populations (endotoxin activated and non-activated) at the attomolar (10⁻¹⁸ moles) level of NO efflux for multiple time points (0 to 4 hr). Furthermore, this type of cellular population data allows for phenotypic correlation between RNS efflux and biophysical properties of each individual cell including refractive index (RI).

RESTULS AND DISCUSSION

The schematics of the flow channel and nanosensor array integration are shown in **Figure**1a. The array is demonstrated using a (AT)₁₅ DNA wrapped SWNT (SWNT/(AT)₁₅), which was previously shown to exhibit nIR intensity attenuation upon selective detection of NO molecules.^{34,35} A commercial microfluidic channel (detail specification in **Table S1**) was coated with micro-droplet of (3-aminopropyl) triethoxysilane (APTES) for self-assembled monolayer formation and nanosensor adhesion on both top and bottom surface of the channel. Stable

dispersions of nanosensors were confirmed via UV-vis-nIR absorption spectra of SWNT/(AT)₁₅ (Figure S1). During evaporation, nanosensor particles necessarily align at the three-phase line of the micro-droplet pinned at the end of the flow channel (Figure S2). This resulted in a uniform sensor array on both top and bottom surfaces of the channel following the Evaporation Induced Self-Assembly (EISA).³⁶ After the EISA process of NO nanosensor, collagen solution (Type I, C3837, Sigma) was injected to make nanosensor array be compatible with cellular adhesion of macrophages.³⁷ Polarized Raman spectroscopy of the completed flow channel showed the depolarization ratio of 0.72 from G band intensity demonstrating that the NO nanosensors were aligned along the flowing direction of channel during EISA (Figure S3).³⁸ There Nanosensor Integrated Microfluidic channels (NIM) were highly transparent to visible light, indicating a uniformly coated nanosensor array without aggregation or large array defects (Figure 1b, left). nIR imaging showed that the NIM displays strong and uniform fluorescence from whole area of the channel (Figure 1b, right). NIM without APTES treatment showed severe nanosensor aggregation during EISA process. Consequently nanosensors were completely removed following PBS flow, indicating that surface chemistry of the microfluidic channel is critically important to uniform and stable EISA process (Figure S4). As the concentration of nanosensor dispersion increases, uniformity of nanosensor array was enhanced with significant decrease of voids and aggregation of nanosensors. The 80 mg/L coating showed the highest nIR intensity with most uniform pixel distributions (Figure S5). We find that NO nanosensors were uniformly coated on the top and bottom surfaces of the channel during EISA, as shown by the comparable nIR pixel distributions along both surfaces. (Figure S6). Peak position and relative peak intensities of nIR spectrum of NIM were almost identical with SWNT in dispersion phase, indicating that the dielectric environment surrounding the immobilized nanosensors were similar (Figure S7).³⁹

Magnified nIR image of NIM with single macrophage size (~20 μm diameter) showed that nanosensors were homogeneously and continuously deposited with approximately 720 local detector pixels across a single cell (**Figure S8**). Atomic force microscopy (AFM) demonstrated that nanosensor bundles were covered on the channel surface at the micron-scale (**Figure S9**). Consequently, the nanosensor array on the microfluidic channel could clearly visualize the macrophages in the channel and maximize the signal-to-noise ratio of the signal from NO efflux for chemical cytometry.³⁷

In-vitro NO detection experiments were conducted to investigate the chemical sensing performance of the NIM. NO solutions were prepared by dilution of diethylenetriamine NONOate solution in PBS. Real-time nIR images of NIM show that the channel nIR emission is quenched with ~20% relative magnitude upon exposure to 10 mM NO flow (**Figure 1d**, top). Nanosensor array shows uniform and near instantaneous nIR intensity response even when imaged at the high-resolution needed to interrogate single cells (20 μ m circled area) (**Figure 1d**, bottom). The nIR pixel histogram demonstrates uniform and overall nIR intensity response to NO flow (**Figure 1e**). Real-time nIR signals (($I_0 - I$)/ I_0) were measured with wide range concentration of NO injection (**Figure 1f**). Here, I_0 and I represent the nIR intensity of the channel at t = 0 and after NO injection, respectively. Upon NO injection, the NIM showed a continuous decrease in nIR signal on the order of 1 - 25% depending on NO concentration. We modeled the sensor response as a first-order reversible reaction where the relationship between the analyte and available binding sites for NO can be described by an equilibrium constant:³⁷

$$K_{\mathbf{A}} = \frac{[A\theta]}{[A][\theta]} \tag{1}$$

Assuming that the sensor response is proportional to the $A\theta/\theta_{tot}$ ratio, it is found that

$$\frac{I - I_0}{I_0} = \alpha \frac{[A\theta]}{[\theta_{\text{tot}}]} + \beta = \alpha \frac{([A]K_A)^n}{([A]K_A)^{n+1}} + \beta \tag{2}$$

with the total concentration of available recognition sites $[\theta]_{tot}$ and the parameter n for cooperativity. Fitting the data in **Figure 1f** with equation (2) ($R^2 = 0.997$) resulted in a proportionality factor $\alpha = 25.64$ with $\beta = -0.42$, $K_D = 1/K_A = 0.00245$ M, and n = 0.878, indicating negatively cooperative binding (n < 1), in good agreement with previous papers.³⁹⁻⁴² This NO detection performance of SWNT/(AT)₁₅ nanosensor is attributed to NO molecules selectively adsorbing on nanotube sidewall donate electrons directly to the conduction bands of SWNT/(AT)₁₅, and extra electrons in the conduction bands can then quench excitons through non-radiative recombination.³⁴

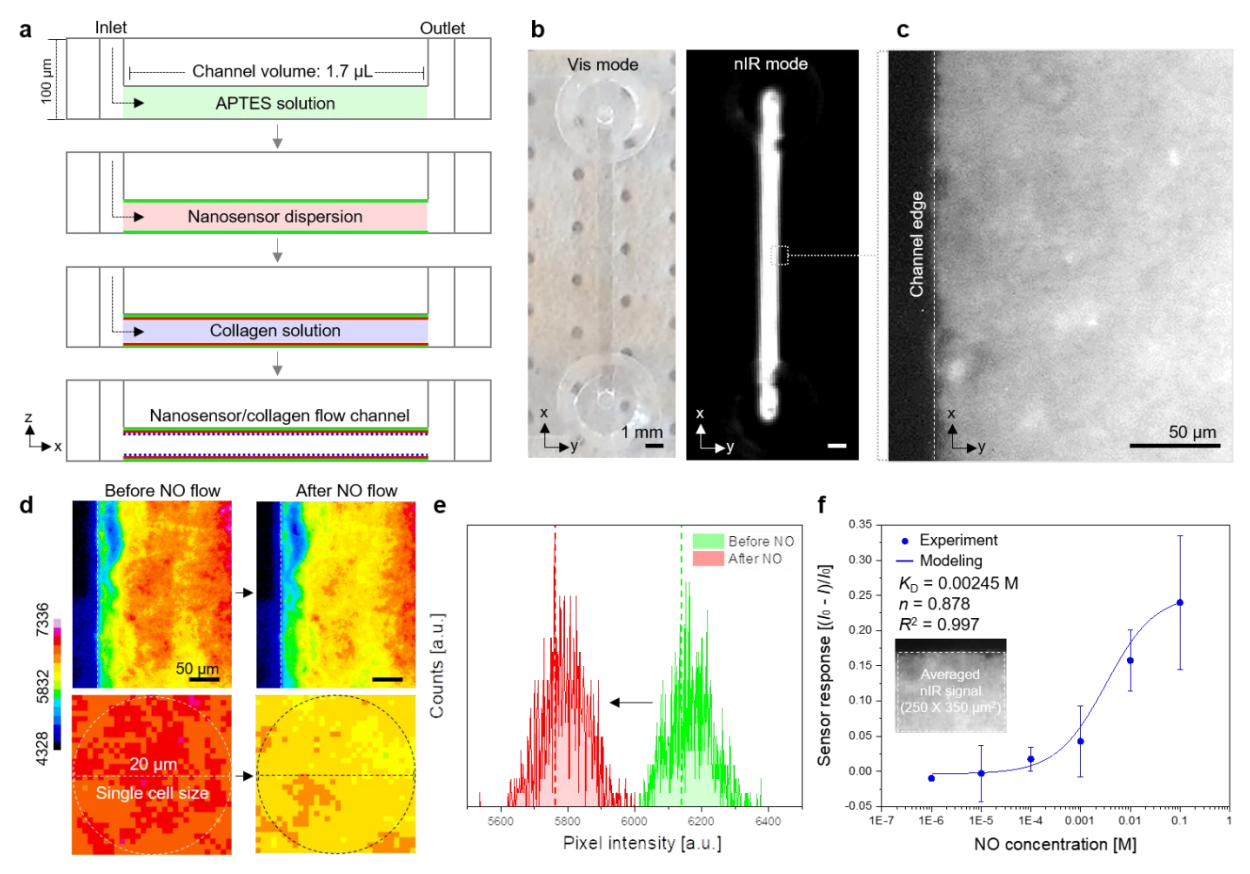


Figure 1. NO nanosensor array integration with microfluidic channel. (a) Schematic illustration of NO nanosensor and collagen layer integration process with microfluidics using EISA. (b) Photograph of completed NIM in visible mode and nIR mode. (c) Magnified nIR image of NIM. (d) nIR snapshots before and after NO flowing (10 mM, 10 min). (e) Intensity histogram of NIM with single macrophage size resolution (20 μm). (f) Maximum response amplitude of NIM with various concentration (10^{-6} , 10^{-5} , 10^{-4} , 10^{-3} , 10^{-2} , 10^{-1} M) of NO injection with cooperative binding model fitting to quantify nanosensor kinetic parameters. The data represent the mean value of 250 × 350 μm² NIM measurement, n = 3.

For the NCC implementation for macrophage monitoring, the NIM was integrated with a syringe pump and nIR microscope. 561 nm excitation laser was provided from the bottom side of the flow channel with dichroic mirror and InGaAs detector (Figure 2a). Target macrophage cells (Raw 264.7, Figure S10) were injected into NIM with 10 µL/min and waited few min for settling on the channel surfaces. Then, cells were adhered on collagen functionalized nanosensor array of NIM (Figure 2b). We found that macrophages in NIM optically interact with the underlying nanosensor emitter array and create a label-free region of highest nIR sensor signal by lensing the photoemission through the adhered macrophage itself (Figure 2c). A magnified nIR image of a single cell showed that the contour and shape of the macrophage could be visualized with highest nIR intensity (I_0) from the nanosensor array corresponding to the center, and Airy rings visible around the periphery. This is attributed to nIR cellular lensing effect by photonic nanojet formation, that we recently discovered. Macrophage cells showed optimum RI ($n_{\text{cell}} = 1.3666 \pm$ 0.0004) and diameter (10 - 20 µm), 43 which is optimum optical condition for the photonic nanojet formation $(n_{\text{cell}}/n_{\text{media}} = 1.028 \ (< 2))$. ⁴⁴ Only the cells on top surface of the channel could be observed with nIR lensing effect since fluorescence from nanosensor array is light source for the photonic nanojet effect (Figure S11). The nIR lensing profiles of macrophages were drastically changed with adhesion on the nanosensor array. Adhered macrophage on nanosensor array apparently displayed the profile of nIR lensing albeit with weaker lensing intensity ($I_{0, \text{ non-ad}} \leq I_{0, \text{ non-ad}}$ $_{ad}$, $\theta_{non-ad} < \theta_{ad}$) and lower refraction angle than non-adhered macrophages due to the relocation of cytoplasmic components along cell elongated axis (Figure 2d).

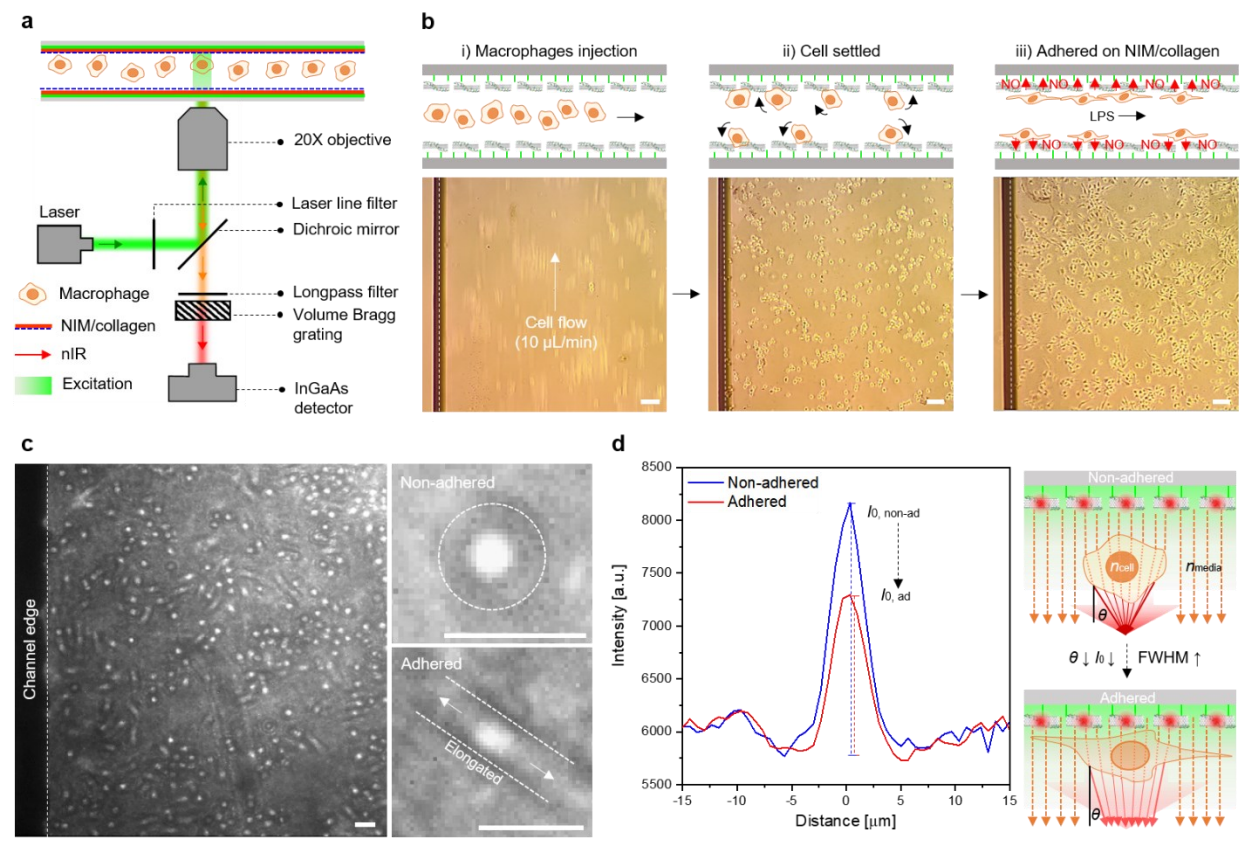


Figure 2. Cellular lensing effect of macrophages in NIM. (a) Schematic illustrations of instrumental setup. (b) Schematics and optical microscope images of macrophages injection and attachment on nanosensor/collagen array in NIM. (c) nIR image of macrophage populations in NIM. Top-right: non-adhered single macrophage. Bottom-right: adhered single macrophage. (d) nIR lensing profiles (left) and schematic illustrations (right) of non-adhered (top) and adhered (bottom) macrophage on nanosensor array. Scale bar: 20 μm.

Finite-difference time-domain (FDTD) numerical modeling demonstrated this nIR lensing behavior of macrophages as originating from a photonic nanojet effect. Micro sized semi-sphere structures having lateral diameters between 8 to 20 µm, cell thickness of 4 µm, and RI values $(n_c/n_m = 1.0275)$ compared with cells were used as targets for the FDTD modeling. The semispherical target was excited by an incident plane wave of wavelength 1 µm corresponding to the fluorescence emission of the SWNT/(AT)₁₅ nanosensor (modeling details in Methods). The resulting optical intensity distribution map showed that light from top surface of the cell strongly focuses at a 22.5 µm distant point from the center of the cell forming a 3 to 4 µm wide fluorescence jet (left, Figure 3a). The numerical model describes the experimental light intensity profile of the macrophage nanojet at 20 μ m focal distance with high fidelity in terms of I_0 , full-with ad halfmaximum (FWHM), including Airy rings (Figure 3b). A slight deviation between the FDTD model and experiment for the Airy rings and FWHM could be possibly originating from the nonuniformity of nIR excitation source and different ellipticity of the macrophages. Modeling demonstrates that as the macrophage more adhered on nanosensor array with larger elongation length (from 8 to 20 µm), nIR light passing through the macrophage is less focused with smaller refraction angles leading to lower enhancement factors (from 2.560 to 1.739) and larger FWHM (from 4.1 to 75 µm) (Figure 3c-3d). nIR lensing profile were measured for multiple macrophages (n = 10) with almost identical FWHM (3.81 µm, $\sigma = 0.28$) and enhancement factors (10.4, $\sigma =$ 3.46) (Figure S12). Furthermore, cellular lensing parameters of macrophages are good agreement in the model from previous work with other various type of cells including lymphocyte, macrophages, epithelial cell, and endothelial cell in terms of FWHM and enhancement factor (Figure S13).7 Overall, nIR lensing phenomenon of macrophages on the nanosensor array are clearly demonstrated and can provide a unique opportunity to cross-correlate the iNOS efflux as measured by the underlying nanosensor array with distinct biophysical properties.

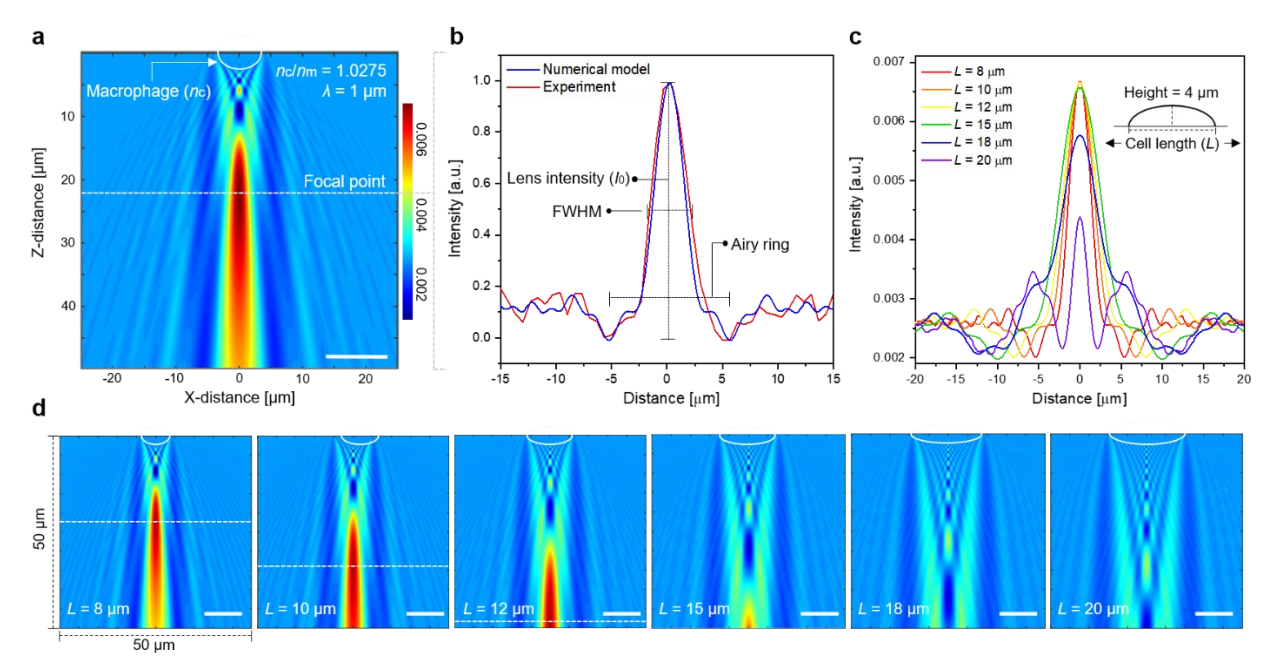


Figure 3. Numerical modeling of macrophage lensing effect. (a) Photonic nanojet model of macrophage and (b) fitting with experimental lensing profile ($n_c/n_m = 1.0275$, $\lambda = 1$ μm, lateral cell length (L) = 8 μm). Solid and dashed white lines indicate the adherend macrophage on nanosensor array and focal points, respectively. (c) Intensity profiles and (d) images of nIR lensing macrophage with different cell length (L = 8, 10, 12, 15, 18, 20 μm with $n_c/n_m = 1.0275$ and $\lambda = 1$ μm) calculated by FDTD model. Enhancement factors are 2.560, 2.546, 2.561, 2.567, 2.275, 1.739 and FWHM are 4.1, 5.1, 6.3, 7.7, 13, 75 μm from left to right. Large simulation (80 X 80 X 80 μm³) domain of L = 15, 18, 20 μm is shown in **Figure S14**.

We found that macrophages in NIM show distinct nIR lensing intensity variations corresponding to different immune activation states. We used lipopolysaccharide (LPS) to induce immune activation of the macrophages, since it is a well known endotoxin for iNOS activation in immune cells *via* mitogen-activated protein (MAP) kinases and nuclear factor kappa B (NF-κB).⁴⁵ Time series nIR snapshots of fixed single cell showed that the I_0 corresponding to the immune activated macrophage (+LPS, Figure 4a) decreased relative to non-activated macrophage (-LPS, Figure 4b) after 4 hr of incubations. The schematic in Figure 4c showed this real-time NO efflux detection mechanism of single cell based on the nIR lensing effect. During the LPS response of macrophage, the NO efflux from cellular iNOS registered on the projected nanosensor area nearest to the cell as an immediate quenching response. This nIR quenching allows for precise quantification of the NO efflux in molecular level. At this point, the nIR lensing power is drastically reduced with weaker fluorescence resulting from the waveguide light source. We modeled the reaction kinetic problem of the NO from the individual cell to translate the observed nIR quenching area above the cell into estimated local NO concentration. The adsorption and desorption of NO on nanosensor array can be described by

$$NO + SWCNT \rightleftarrows H_2O_2 - SWCNT \tag{3}$$

Corresponding to the rate expression:³⁵

$$\frac{d[\text{NO-SWNT}]}{dt} = k_{\text{f}}[\text{NO}][\text{SWCNT}] - k_{\text{r}}[\text{NO-SWNT}]$$
(4)

where k_f , k_r are the forward and backward rate constants, respectively, and ratio between k_f and k_r was calculated from the effective equilibrium dissociation constant $K_D = 0.00245$ M. Since the nIR intensity of the nanosensor array is proportional to the fraction of unoccupied sites for binding,

$$I/I_0 = [SWCNT]/[SWCNT]_0$$
 (5)

The local concentration of NO detected by the nanosensor array involves the measured intensity (*I*) and its time-derivative

$$[NO] = \frac{1}{k_f} \frac{I_0}{I} \left[k_r \left(1 - \frac{I}{I_0} \right) - \frac{1}{I_0} \frac{dI}{dt} \right] \tag{6}$$

Integrating equation (8) yields

$$I(t) = \frac{I_0}{k_s} (k_r + k_f [NO] e^{-k_s t})$$
(7)

$$k_s = k_r + k_f[NO] (8)$$

Thus, equation (7) can be utilized to estimate the local NO concentration of each single cell from the measured nIR intensity (**Figure 4d**). The +LPS group (n = 79) showed mean estimated NO efflux rate of 570 attomole/cell·hr, which is 1.66- and 1.46-times higher efflux than -LPS and +LPS & aminoguanidine (AG) groups. Here, AG, a selective iNOS inhibitor, suppresses the NO signal as a negative control.⁴⁶ We detected a basal NO level even for the non-activated macrophages without LPS activation (-LPS), which is consistent with the literature.⁴⁷ This showed that our NIM platform can inform heterogeneities in the iNOS process within macrophage cell populations.

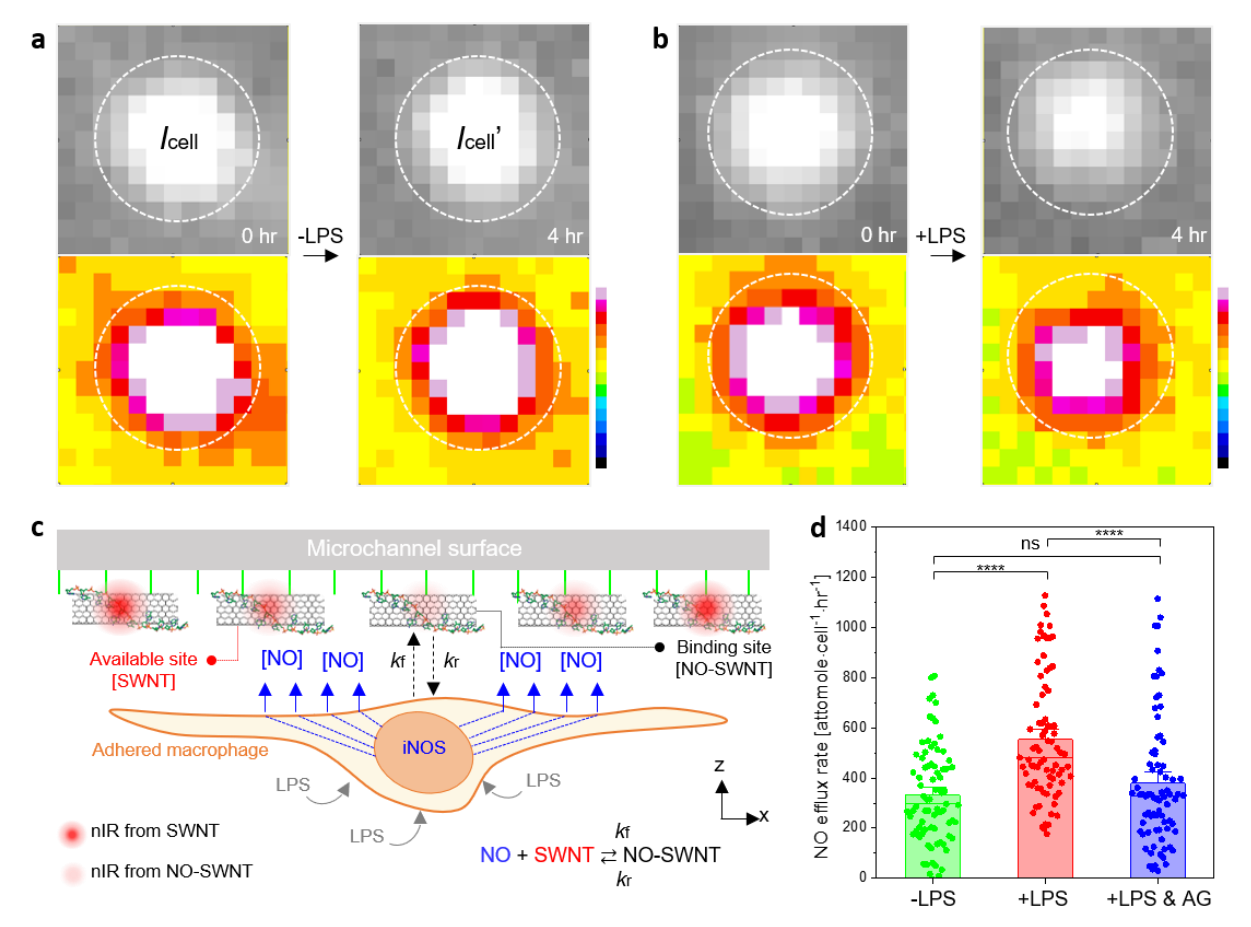


Figure 4. Real-time NO efflux monitoring of macrophages with endotoxin activation. nIR lensing responses with NO efflux from (a) non-activated (-LPS) and (b) activated macrophage (+LPS, 10 μ g/mL, 4 hr). 16-color scalebars represent nIR intensity from white (5780) to dark blue (4387). (c) Reaction kinetic modeling for translation of measured nIR signals to real-time local NO concentration. (d) Sensor response statistics of the cells with different activation states. Data are mean \pm standard error, with $n_{\text{cell}} = 79$ from n = 2 biologically independent samples. p values were calculated using one-way analysis of variance (ANOVA), followed by Tukey analysis (****p < 0.0001, ns = 0.4846).

The combination of cellular lensing and label-free nanosensor monitoring within a microfluidic channel allowed for real-time NO efflux cytometry of distinct macrophage populations, such as those that are immune activated (+LPS) compared to non-activated (-LPS) (Figure 5). We show that our NCC platform collects a multivariate data set for each individual macrophage within the population, that we then extract and evaluate with the aid of automated multi-channel measurements (Figure S15). The results allowed us to plot the real-time NO efflux rates of two distinct groups (n = 321 for -LPS, n = 405 for +LPS) versus key biophysical attributes of each individual macrophage such as RI. Since the immune activation of macrophages is based on iNOS with cellular relocation, RI indicating intracellular components variation due to membrane mechanistic would be key physical variables of macrophage NO responses. Therefore, we specifically chose the RI to correlate them with NO secretion to precisely figure out the macrophage iNOS heterogeneity.

We plot the single cell distribution curves for real-time NO efflux rates and RI of two macrophage groups. Upon LPS activations, the average NO efflux rate of macrophage population was elevated by 35% with a 3% larger increase in the heterogeneity compared to non-activated populations (**Figure 5a**). The NIM allowed us to quantify the mean NO efflux rates of these two populations as 342 and 464 attomole/cell·min with σ of 199 and 206 attomole/cell·min for -LPS and +LPS, respectively. These measured NO efflux rates from NIM were similar with the ranges previously reported for identical macrophage NO efflux rate from 10 to 300 attomole/cell·min from the commercial NO assay kit (Griess method) for the precise comparison (**Figure S16**). The mean values are in good agreement for the NIM experiments and commercial assay demonstrating that

our approach is reliable in this way and allows the investigation of cellular parameters of a subpopulation in real-time.

There is a distinct change in the RI distribution upon LPS activation, with trimodal subpopulations observed for activated macrophages with a mean of 1.359 (σ = 0.015) but a single distribution with higher mean of 1.366 μ m² (σ = 0.009) before immune activation (**Figure 5b**). This is attributed to that LPS activated macrophages started to be adhered and elongated along nanosensor array and release the NO molecules drastically with distributed cytoplasm due to the production of iNOS.⁴⁹ Accordingly, nIR refraction through the cell is less focused by photonic nanojet formation.⁵⁰ Notably, this measured RI variations of macrophages from our NCC platform was within the range previously reported for macrophages RI characterization.⁴³ This observation is important because one requires single cell resolution in order to quantify this type of biophysical change, underscoring an advantage of this NCC platform. This ability to detect and analyze subpopulations from a cellular population undergoing biofunctional changes has significant advantages in analytical biochemistry.

We plot the cytometry graph correlating real-time NO efflux rates versus RI of each single macrophage (**Figure 5c**). With LPS activation, we find that the mean NO efflux rate of macrophage increases along with a widening of the distribution, and this occurs with a decrease of RI. **Figure 5d** summarizes the variation in macrophage characteristics before and after the immune activation process that we characterized. Real-time NO efflux rate of macrophage populations showed 35.7% elevation and the RI of the populations decreased by -0.51% scale. This cellular mechanistic insight may lead to additional methods of sorting macrophage populations.

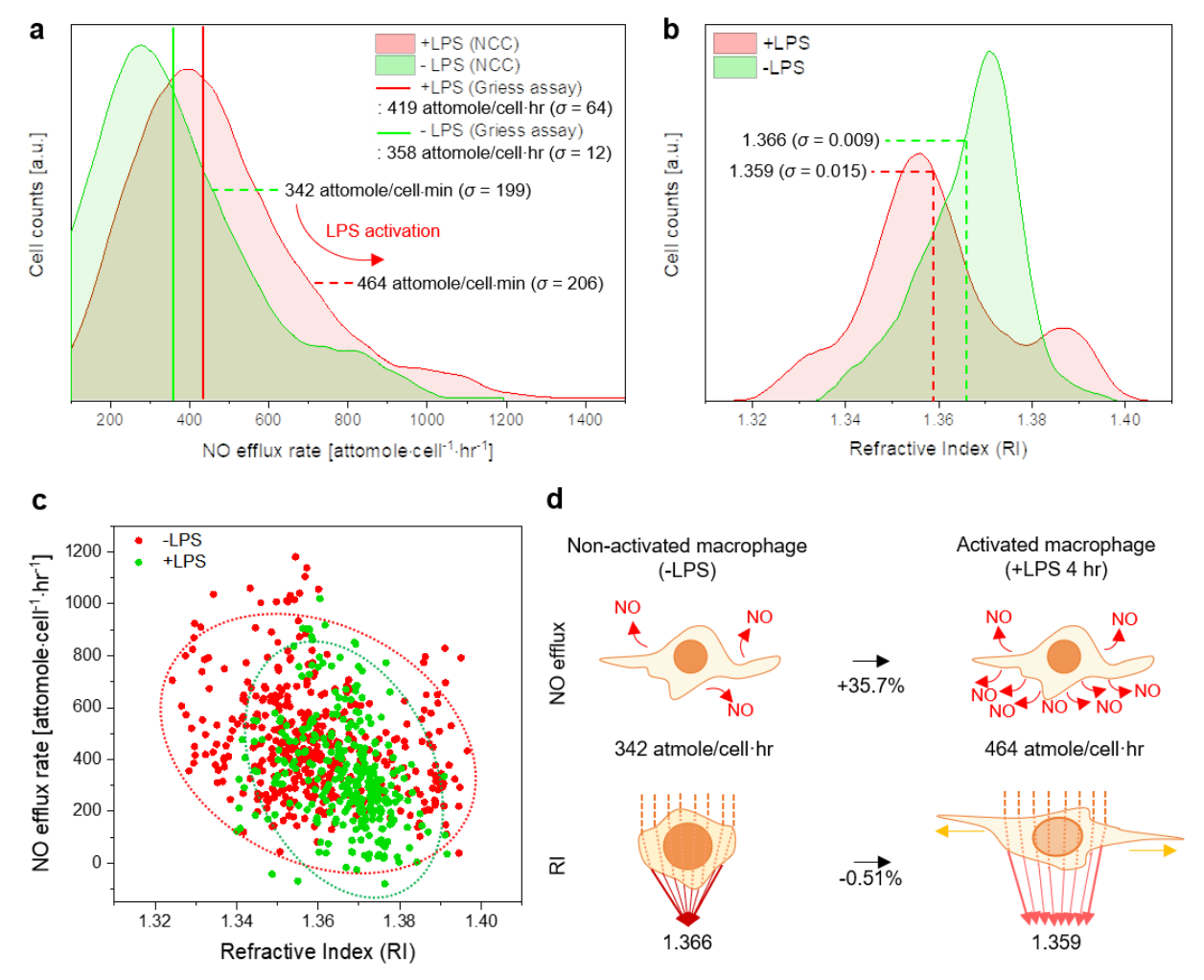


Figure 5. NCC for monitoring of multimodal iNOS heterogeneity of macrophages. Data are n_{cell} = 321 for -LPS, n_{cell} = 405 for +LPS from n = 7 biologically independent samples. (a) Distribution curves for NO efflux rates of non-activated (-LPS) and activated (+LPS, 4 hr) macrophages with data from commercial assay kit (Griess assay, solid lines). Griess assay data are from n = 3 biologically independent samples. (b) Distribution curves for RI of non-activated (-LPS) and activated (+LPS, 4 hr) macrophages (c) Cytometry plots of macrophage populations. Dashed circles represent the 2D confidence ellipse with 95% confidence level. (d) Schematics illustrations for cell properties variations of macrophage populations with immune activations.

CONCLUSIONS

In conclusion, we demonstrated a macrophage population monitoring system based on nanosensor array integrated microfluidics. Using this platform, large number of single macrophages can be imaged and analyzed on the array via their projected nIR lensing image, producing a profile that matched the predictions of a photonic nanojet model. With this biophotonic property, NO efflux profiles of macrophages from iNOS were label-free monitored in real-time at the attomolar level. We used this tool to study the heterogeneity of the immune response of distinct macrophage populations at in a completely non-destructive manner. We find that real-time NO efflux of macrophages is heterogeneous and distinctly related to biophysical parameter following endotoxin activation. Our measurements showed that non-activated and activated macrophage populations released 342 and 464 attomole/cell·hr with a 3% larger increase in the heterogeneity, and estimated RI of macrophage decrease from 1.366 to 1.359 with trimodal subpopulations under LPS activation. We envision that this nanotechnology based biophotonic cytometer provides a unique strategy for coupling nanosensors into a format that allows single cell analysis of relevant populations for cellular manufacturing, cellular immunology, and biopharmaceutical research.

METHODS

Preparation and characterization of nanosensors. HiPcoTM SWNTs purchased from Unidym were suspended with a 30-base (dAdT) sequence of ssDNA (Integrated DNA Technologies) in a 2:1 DNA:SWNT mass ratio in 0.1 M NaCl. A typical DNA concentration was 2 mg/mL. Samples were sonicated with a 3 mm probe tip (Cole Parmer) for 10 min at a power of 10 W and 40% amplitude in an ice bath. Then samples were centrifuged twice for 90 min (Eppendorf Centrifuge

5415D) at 16100 RCF (Relative Centrifugal Force). Afterwards, the supernatant was collected and the pellet was discarded. UV-Vis-nIR absorption spectra were collected to verify successful suspension. Nanosensor (SWNT/(AT)₁₅) concentration in the dispersion was estimated using an extinction coefficient of $\mathcal{E}_{632 \text{ nm}} = 0.036 \text{ (mg/L)}^{-1}$. Final concentration of SWNT/(GT)₁₅ is from 10 to 80 mg/L. 80 mg/L concentration of nanosensor dispersion was used to all NIM experiments. Nanosensors integration with microfluidic channel. Microfluidic channels were purchased from ibidi^R (μ-Slide VI 0.1, ibiTreat). 2 μL of APTES (99%, Sigma Aldrich) in ethanol (1% APTES, 1% H₂O) was injected to microfluidic channel with micro-pipetting and treated for 3 hr. After APTES treatment, 2 µL of nanosensor dispersions were injected. After overnight evaporation, SWNT/(AT)₁₅ coated channel surfaces were rinsed with 1 mL 1X PBS (pH 7.4, Life TechnologiesTM) twice to remove unbounded SWNT/(AT)₁₅. Before cell injection, collagen solution (Type I, C3837, Sigma) was injected and incubated in humidified 37°C chamber to make nanosensor array compatible with macrophage adhesion. After collagen layer incubation, the flow channel was flushed with PBS again to remove unbounded residual nanosensors and collagen particles. Silicone tubes were connected with NIM using Elbow Luer Connector Male (ibidi^R). Invitro NO detection experiments were conducted as below. DETA NONOate ((Z)-1-[N-(2aminoethyl)-N-(2-ammonioethyl)amino|diazen-1-ium-1,2-diolate, **VWR** Scientific) dissolved with 1X PBS from 1 µM to 0.1 M to investigate sensing performance of NIM. Diluted NO solutions were flowing through the NIM with syringe pump and quenching signals from nanosensor array were recorded for 600 sec. Recorded nIR images were processed by ImageJ with Gray and Fire scales to clearly visualize the variations of nIR intensities.

Characterizations and nIR measurements. UV-Vis-nIR absorption spectra were measured for both nanosensor solutions and NIM (Cary 5000, Agilent Technologies, Inc). AFM profiles of

nanosensor array were scanned with Bruker Multimode 8 with Controller V. AFM images were taken in the ScanAsyst tapping mode in the air with TESPA probes having an elastic constant of 42 N/m and tip radius of 8 nm. The images were recorded with the scan rate of 1 Hz and resolution of 1024 lines per image. Image analysis was done with Nanoscope Analysis software 1.4 from Bruker. nIR spectra were collected with a fluorescence spectrometer equipped with a 785 nm photodiode laser (B&W Tek. Inc. 450 mW) and imaged using a Zeiss AxioVision inverted microscope with appropriate optical filters. The fluorescence passed through an Acton SP2500 spectrometer (Princeton Instruments), and measured with a liquid nitrogen cooled InGaAs 1D detector (Princeton Experiments). Inverted OM (Eclipse TS100, Nikon) was used for NIM and flowing cell imaging with visible light. nIR lensing effect and NO efflux cytometry were observed and recorded by nIR microscopy hyperspectral imager (IMA IRTM, Photon Etc.). 561 nm laser (MGL-FN-561, Opto Engine LLC) passed the laser line filter and reflected by dichroic mirror. Laser power was controlled from 30 mW to 350 mW with laser line filtering. Reflected excitation laser entered the objective and touch the NIM for releasing nIR from the nanosensor array. nIR fluorescence from NIM passed the both longpass filter and volume Bragg grating, and measured with a liquid nitrogen cooled InGaAs 1D detector (Princeton Experiments). All the measurements were conducted with 20X objective, 0.1 exposure time and medium intensity gain.

FDTD simulations. FDTD simulations for nIR photonic nanojet were performed using Lumerical FDTD Solution. Micro sized semi-spherical structures having various range of elongation length (radius: 8, 10, 12, 15, 18, 20 μ m) and RI (n_c/n_m : 1.0275) were set and excited by an incident plane wave with a wavelength of 1000 nm, corresponding to the fluorescence emission of the nanosensor array. The simulation domains were 50 X 50 X 50 μ m³ and 80 X 80 X 80 μ m³, and uniform mesh

of around 30 nm was used. The perfectly matched layers (PML) were arranged around the boundaries. RI of media (out of macrophage) was set to 1.33.

Cell experiments. Raw 264.7 (ATCC TIB-71TM) cells were purchased from American Type Culture Collection (ATCC) and cultivated according to the supplier's protocol with medium consisting of ATCC-formulated Dulbecco's Modified Eagle's Medium (30-2002) and 10% of fetal bovine serum (FBS) (Life Technologies). Cells were cultured in 75 cm² cell culture flasks (Falcon) under incubating conditions of 5% CO₂ at 37°C. To measure the NO efflux from the cells, three days cultured Raw 264.7 media were used (cell number: 10⁵ - 10⁶/mL) and all the culturing media with cells were centrifuged with 10 min 130 RCF at 10°C to remove all the by-product, accumulated efflux and abnormal cells in media. 10 µL of 1 mg/mL LPS (Lipopolysaccharides from Escherichia coli O55:B5) was added in macrophage media to activate the cells to release the NO. Aminoguanidine hydrochloride ($\geq 98\%$) was used to iNOS inhibitor as a negative control. Non-activated macrophage cells were injected through NIM using syringe pump (Harvard Apparatus) and incubated for overnight to be adhered on collagen functionalized nanosensor array. NO efflux cytometry was conducted for fixed region of each channel (1, 2, 3, 4) waiting 4 hr efflux waiting. n = 7 biological replicates of macrophage populations were used for cytometry experiments.

ASSOCIATED CONTENT

Supporting Information. The following files are available free of charge. Specifications of commercial microfluidic channel. Photograph and UV-vis-nIR absorption spectra of SWNT/(AT)₁₅ nanosensor dispersions. Time-series photograph of EISA process. Polarized Raman spectrum of NIM. nIR mapping of NIM without ATPES treatment for EISA. Nanosensor

concentration effects on ESIA process. nIR pixel histogram of top and bottom NIM. nIR

fluorescnece spectrum of NIM. Uniformity of nanosensor array in microfluidic channel. AFM

characterizations of nanosensor array within microfluidic channel. Optical microscope images of

macrophages culturing for the whole experiments. nIR image of bottom and top surface of

macrophage injected NIM. nIR intensity profiles of multiple macrophages. Lensing parameters of

macrophage fitted with numerical model from previous work. FDTD modeling results for nIR

photonic nanojet effect of macrophage with various elongation length. Parallel NIM approaches.

Griess assay experimental procedures and resulting data.

AUTHOR INFORMATION

Corresponding Author

* Email: strano@mit.edu

Author Contributions

S.-Y. C. and M. S. S. conceived the idea, designed the project and planned experiments with the

assistance of V. B. K., X. G., S. J. M., P. G. S.-Y. C. prepared the nanosensors, fabricated the NIM,

implemented the cytometry with cell culturing, measured and analyzed the data. V. B. K.

conducted FDTD numerical modeling for photonic nanojet demonstration. S. J. M. assisted

commercial NO assay. P. G. assisted with AFM characterization of nanosensor array. S.-Y. C. and

M. S. S. wrote the manuscript with inputs from all the authors. All authors contributed to

discussions informing the research.

ORCID

Soo-Yeon Cho: 0000-0001-6294-1154

Xun Gong: 0000-0003-4168-2768

25

Michael S. Strano: 0000-0003-2944-808X

Notes

The authors declare no competing interest.

ACKNOWLEDGEMENT

The authors are grateful for financial support from Bose Fellowship Award to M. S. S., funding

from the Disruptive & Sustainable Technology for Agricultural Precision (DiSTAP) and the

Singapore MIT Alliance for Research and Technology (SMART) Center.

ABBREVIATIONS

RNS, Reactive nitrogen species; NO, nitric oxide; iNOS, inducible nitric oxide synthase; NCC,

nanosensor chemical cytometry; nIR, near infrared; SWNT, single-walled carbon nanotube;

APTES, (3-aminopropyl) triethoxysilane; NIM, nanosensor integrated microfluidic; AFM, atomic

force microscopy; FDTD, finite-difference time-domain; LPS, lipopolysaccharide; MAP,

mitogen-activated protein; NF-kB, kinases and nuclear factor kappa B; AG, aminoguanidine;

ANOVA, analysis of variance

REFERENCES

(1) West, A. P.; Brodsky, I. E.; Rahner, C.; Woo, D. K.; Erdjument-Bromage, H.; Tempst, P.;

Walsh, M. C.; Choi, Y.; Shadel, G. S.; Ghosh, S. TLR Signalling Augments Macrophage

Bactericidal Activity Through Mitochondrial ROS. *Nature* **2011**, *472*, 476-480.

(2) Thomas, D. D.; Ridnour, L. A.; Isenberg, J. S.; Flores-Santana, W.; Switzer, C. H.; Donzelli,

S.; Hussain, P.; Vecoli, C.; Paolocci, N.; Ambs, S.; Colton, C. A.; Harris, C. C.; Roberts, D. D.;

26

- Wink, D. A. The Chemical Biology of Nitric Oxide: Implications in Cellular Signaling. *Free Radical Biol. Med.* **2008**, *45*, 18-31.
- (3) Varin, A.; Gordon, S. Alternative Activation of Macrophages: Immune Function and Cellular Biology. *Immunobiology* **2009**, *214*, 630-641.
- (4) Gordon, S. Alternative Activation of Macrophages. *Nat. Rev. Immunol.* **2003**, *3*, 23-35.
- (5) Qian, C.; Yun, Z.; Yao, Y.; Cao, M.; Liu, Q.; Hu, S.; Zhang, S.; Luo, D. Heterogeneous Macrophages: Supersensors of Exogenous Inducing Factors. *Scand. J. Immunol.* **2019**, *90*, e12768.
- (6) Landhuis, E. Single-cell approaches to immune profiling. *Nature* **2018**, *557*, 595-597.
- (7) Cho, S.-Y.; Gong, X.; Koman, V.; Kuehne, M.; Moon, S. J.; Son, M.; Lew, T. T. S.; Gordiichuk, P.; Jin, X.; Sikes, H. D.; Strano, M. S. Cellular Lensing and nIR Fluorescent Nanosensor Array Enable Chemical Efflux Cytometry. *Nat. Commun.* **2021**, *12*, 3079.
- (8) Gordon, S.; Plüddemann, A. Tissue macrophages: heterogeneity and functions. *BMC Biol.* **2017**, *15*, 53.
- (9) Wynn, T. A.; Vannella, K. M. Macrophages in Tissue Repair, Regeneration, and Fibrosis. *Immunity* **2016**, *44*, 450-462.
- (10) Stern, A. M.; Zhu, J. An Introduction to Nitric Oxide Sensing and Response in Bacteria. *Adv. Appl. Microbiol.* **2014**, *87*, 187-220.
- (11) Wilson, H. M. Macrophages Heterogeneity in Atherosclerosis Implications for Therapy. *J. Cell. Mol. Med.* **2010**, *14*, 2055-2065.
- (12) Colton, C. A. Heterogeneity of Microglial Activation in The Innate Immune Response in The Brain. *J. Neuroimmune Pharmacol.* **2009**, *4*, 399-418.

- (13) Satija, R.; Shalek, A. K. Heterogeneity in Immune Responses From Populations to Single Cells. *Trends. Immunol.* **2014**, *35*, 219-229.
- (14) Dash, P.; McClaren, J. L.; Oguin III, T. H.; Rothwell, W.; Todd, B.; Morris, M. Y.; Becksfort, J.; Reynolds, C.; Brown, S. A.; Doherty, P. C.; Thomas, P. G. Paired Analysis of TCRα and TCRβ Chains at The Single-Cell Level in Mice. *J. Clin. Invest.* **2011**, *121*, 288-295.
- (15) Metto, E. C.; Evans, K.; Barney, P.; Culbertson, A. H.; Gunasekara, D. B.; Caruso, G.; Hulvey, M. K.; da Silva, J. A. F.; Lunte, S. M.; Culbertson, C. T. An Integrated Microfluidic Device for Monitoring Changes in Nitric Oxide Production in Single T-lymphocyte (Jurkat) Cells. *Anal. Chem.* **2013**, *85*, 10188-10195.
- (16) Hunter, R. A.; Storm, W. L.; Coneski, P. N.; Schoenfisch, M. H. Inaccuracies of nitric oxide measurement methods in biological media. *Anal. Chem.* **2013**, *85*, 1957-1963.
- (17) Brown, M. D.; Schoenfisch, M. H. Selective and Sensocompatible Electrochemical Nitric Oxide Sensor with a Bilaminar Design. *ACS Sens.* **2019**, *4*, 1766-1773.
- (18) Cohen, D.; Dickerson, J. A.; Whitmore, C. D.; Turner, E. H.; Palcic, M. M.; Hindsgaul, O.; Dovichi, N. J. Chemical Cytometry: Fluorescence-Based Single-Cell Analysis. *Annu. Rev. Anal. Chem.* **2008**, *1*, 165-190.
- (19) Oomen, P. E.; Aref, M. A.; Kaya, I.; Phan, N. T. N.; Ewing, A. G. Chemical Analysis of Single Cells. *Anal. Chem.* **2019**, *91*, 588-621.
- (20) Mainz, E. R.; Gunasekara, D. B.; Caruso, G.; Jensen, D. T.; Hulvey, M. K.; da Silva, J. A. F.; Metto, E. C.; Culbertson, A. H.; Culbertsong, C. T.; Lunte, S. M. Monitoring Intracellular Nitric Oxide Production Using Microchip Electrophoresis and Laser-Induced Fluorescence Detection. *Anal. Methods* **2012**, *4*, 414-420.

- (21) Caruso, G.; Fresta, C. G.; Siegel, J. M.; Wijesinghe, M. B.; Lunte, S. M. Microchip Electrophoresis with Laser-Induced Fluorescence Detection for The Determination of The Ratio of Nitric Oxide to Superoxide Production in Macrophages During Inflammation. *Anal. Bioanal. Chem.* **2017**, *409*, 4529-4538.
- (22) Vickerman, B. M. Anttila, M. M.; Petersen, B. V.; Allbritton, N. L.; Lawrence, D. S. Design and Application of Sensors for Chemical Cytometry. *ACS Chem. Biol.* **2018**, *13*, 1741-1751.
- (23) Roach, K. L.; King, K. R.; Uygun, B. E.; Kohane, I. S.; Yarmush, M. L.; Toner, M. High Throughput Single Cell Bioinformatics. *Biotechnol, Prog.* **2009**. 25, 1772-1779.
- (24) Jin, P.; Wiraja, C.; Zhao, J.; Zhang, J.; Zheng, L.; Xu, C. Nitric Oxide Nanosensors for Predicting the Development of Osteoarthritis in Rat Model. *ACS Appl. Mater. Interfaces* **2017**, *9*, 25128-25137.
- (25) Ramesh, A.; Kumar, S.; Brouillard, A.; Nandi, D.; Kulkarni, A. A Nitric Oxide (NO) Nanoreporter for Noninvasive Real-Time Imaging of Macrophage Immunotherapy. *Adv. Mater.* **2020**, *32*, 2000648.
- (26) Jiang, S.; Cheng, R.; Wang, X.; Xue, T.; Liu, Y.; Nel, A.; Huang, Y.; Duan, X. Real-time electrical detection of nitric oxide in biological systems with sub-nanomolar sensitivity. *Nat. Commun.* **2013**, *4*, 2225.
- (27) Brown, M. D.; Schoenfisch, M. H. Selective and Sensocompatible Electrochemical Nitric Oxide Sensor with a Bilaminar Design. *ACS Sens.* **2019**, *4*, 1766-1773.
- (28) Li, R.; Qi, H.; Ma, Y.; Deng, Y.; Liu, S.; Jie, Y.; Jing, J.; He, J.; Zhang, X.; Wheatley, L.; Huang, C.; Sheng, X.; Zhang, M.; Yin, L. A flexible and physically transient electrochemical sensor for real-time wireless nitric oxide Monitoring. *Nat. Commun.* **2020**, *11*, 3207.

- (29) Farrera, C.; Andón, F. T.; Feliu, N. Carbon Nanotubes as Optical Sensors in Biomedicine. *ACS Nano* **2017**, *11*, 10637-10643.
- (30) Munawar, A.; Ong, Y.; Schirhagl, R.; Tahir, M. A.; Khanae, W. S.; Bajwa, S. Z. Nanosensors for Diagnosis with Optical, Electric and Mechanical Transducers. *RSC Adv.* **2019**, *9*, 6793-6803.
- (31) Almeida, B.; Rogers, K. E.; Nag, O. K.; Delehanty, J. B. Sensing Nitric Oxide in Cells: Historical Technologies and Future Outlook. *ACS Sens.* **2021**, doi.org/10.1021/acssensors.1c00051
- (32) Abdel-Karim, R.; Reda, Y.; Abdel-Fattah, A. Review-Nanostructured Materials-Based Nanosensors. *J. Electrochem. Soc.* **2020**, *167*, 037554.
- (33) Kozawa, D.; Cho, S.-Y.; Gong, X.; Nguyen, F. T.; Jin, X.; Lee, M. A.; Lee, H.; Zeng, A.; Xue, G.; Schacherl, J.; Gibson, S.; Vega, L.; Strano, M. S. A Fiber Optic Interface Coupled to Nanosensors: Applications to Protein Aggregation and Organic Molecule Quantification. *ACS Nano* **2020**, *14*, 10141-10152.
- (34) Zhang, J.; Boghossian, A. A.; Barone, P. W.; Rwei, A.; Kim, J.-H.; Lin, D.; Heller, D. A.; Hilmer, A. J.; Nair, N.; Reuel, N. F.; Strano, M. S. Single Molecule Detection of Nitric Oxide Enabled by d(AT)₁₅ DNA Adsorbed to Near Infrared Fluorescent Single-Walled Carbon Nanotubes. *J. Am. Chem. Soc.* **2011**, *133*, 567-581.
- (35) Ulissi, Z. W.; Sen, F.; Gong, X.; Sen, S.; Iverson, N.; Boghossian, A. A.; Godoy, L. C.; Wogan, G. N.; Mukhopadhyay, D.; Strano, M. S. Spatiotemporal Intracellular Nitric Oxide Signaling Captured Using Internalized, Near-Infrared Fluorescent Carbon Nanotube Nanosensors. *Nano Lett.* **2014**, *14*, 4887-4894.

- (36) Engel, M.; Small, J. P.; Steiner, M.; Freitag, M.; Green, A. A.; Hersam, M. C.; Avouris, P. Thin Film Nanotube Transistors Based on Self-Assembled, Aligned, Semiconducting Carbon Nanotube Arrays. *ACS Nano* **2008**, *2*, 2445-2452.
- (37) Kruss, S.; Salem, D. P.; Vuković, L.; Lima, B.; Ende, E. V.; Boyden, E. S.; Strano, M. S. High-Resolution Imaging of Cellular Dopamine Efflux Using a Fluorescent Nanosensor Array. *Proc. Natl. Acad. Sci. U.S.A.* **2017**, *114*, 1789-1794.
- (38) Cho, S.-Y.; Yu, H.; Choi, J.; Kang, H.; Park, S.; Jang, J.-S.; Hong, H.-J.; Kim, I.-D.; Lee, S.-K.; Jeong, H. S.; Jung, H.-T. Continuous Meter-Scale Synthesis of Weavable Tunicate Cellulose/Carbon Nanotube Fibers for High-Performance Wearable Sensors. ACS Nano 2019, 13, 9332-9341.
- (39) Lee, M. A.; Nguyen, F. T.; Scott, K.; Chan, N. Y. L.; Bakh, N. A.; Jones, K. K.; Pham, C.; Garcia-Salinas, P.; Garcia-Parraga, D.; Fahlman, A.; Marco, V.; Koman, V. B.; Oliver, R. J.; Hopkins, L. W.; Rubio, C.; Wilson, R. P.; Meekan, M. G.; Duarte, C. M.; Strano, M. S. Implanted Nanosensors in Marine Organisms for Physiological Biologging: Design, Feasibility, and Species Variability. *ACS Sens.* **2019**, *4*, 32-43.
- (40) Kruss, S.; Landry, M. P.; Ende, E. V.; Lima, B. M. A.; Reuel, N. F.; Zhang, J.; Nelson, J.; Mu, B.; Hilmer, A.; Strano, M. S. Neurotransmitter Detection Using Corona Phase Molecular Recognition on Fluorescent Single-Walled Carbon Nanotube Sensors. *J. Am. Chem. Soc.* **2014**, *136*, 713-724.
- (41) Lew, T. T. S.; Koman, V. B.; Silmore, K. S.; Seo, J. S.; Gordiichuk, P.; Kwak, S.-Y.; Park, M.; Ang, M. C.-Y.; Khong, D. T.; Lee, M. A.; Chan-Park, M. B.; Chua, N.-H.; Strano, M. S. Real-Time Detection of Wound-Induced H₂O₂ Signalling Waves in Plants with Optical Nanosensors. *Nat. Plants* **2020**, *6*, 404-415.

- (42) Heller, D. A.; Jin, H.; Martinez, B. M.; Patel, D.; Miller, B. M.; Yeung, T.-K.; Jena, P V.; Höbartner, C.; Ha, T.; Silverman, S. K.; Strano, M. S. Multimodal Optical Sensing and Analyte Specificity Using Single-Walled Carbon Nanotubes. *Nat. Nanotechnol.* **2009**, *4*, 114-120.
- (43) Baczewska, M.; Eder, K.; Ketelhut, S.; Kemper, B.; Kujawińska, M. Refractive Index Changes of Cells and Cellular Compartments Upon Paraformaldehyde Fixation Acquired by Tomographic Phase Microscopy. *Cytometry A.* **2021**, *99*, 388-398.
- (44) Heifetz, A.; Kong, S.-C.; Sahakian, A. V.; Taflove, A.; Backman, V. Photonic Nanojets. *J. Comput. Theor. Nanosci.* **2009**, *6*, 1979-1992.
- (45) Hwang, J.-S.; Kwon, M.-Y.; Kim, K.-H.; Lee, Y.; Lyoo, I. K.; Kim, J. E.; Oh, E.-S.; Han, I.-O. Lipopolysaccharide (LPS)-stimulated iNOS Induction Is Increased by Glucosamine under Normal Glucose Conditions but Is Inhibited by Glucosamine under High Glucose Conditions in Macrophage Cells. *J. Biol. Chem.* **2017**, *292*, 1724-1736.
- (46) Jiang, S.; Cheng, R.; Wang, X.; Xue, T.; Liu, Y.; Nel, A.; Huang, Y.; Duan, X. Real-time Electrical Detection of Nitric Oxide in Biological Systems With Sub-Nanomolar Sensitivity. *Nat. Commun.* **2013**, *4*, 2225.
- (47) Wu, F.; Zhou, C.; Zhou, D.; Ou, S.; Liu, Z.; Huang, H. Immune-Enhancing Activities of Chondroitin Sulfate in Murine Macrophage RAW 264.7 Cells. *Carbohydr. Polym.* **2018**, *198*, 611-619 (2018).
- (48) Yao, H.-W.; Guo, X.-F.; Wang, H. Simultaneous Quantitation of Intra- and Extracellular Nitric Oxide in Single Macrophage RAW 264.7 Cells by Capillary Electrophoresis with Laser-Induced Fluorescence Detection. *Anal. Chem.* **2020**, *92*, 11904-11911.
- (49) McWhortera, F. Y.; Wanga, T.; Nguyena, P.; Chunga, T.; Liu, W. F. Modulation of macrophage phenotype by cell shape. *Proc. Natl. Acad. Sci. U. S. A.* **2013**, *110*, 17253-17258.

(50) Liu, P. Y.; Chin, L. K.; Ser, W.; Chen, H. F.; Hsieh, C.-M.; Lee, C.-H.; Sung, K.-B.; Ayi, T. C.; Yap, P. H.; Liedberg, B.; Wang, K.; Bourouinaj, T.; Leprince-Wang, Y. Cell Refractive Index for Cell Biology and Disease Diagnosis: Past, Present and Future. *Lab Chip.* **2016**, *16*, 634-644.

For Table of Contents Only

